Kovove Mater. 59 2021 11–20
DOI: 10.4149/km_2021_1_11

Effect of rare earth Y on properties of Zr-based bulk metallic glasses

J.-L. Li[1,2], C.-Y. Li[1,2]*, S.-P. Wang[1], H.-B. Wang[1], S.-Z. Kou[1,2]

[1]*State Key Laboratory of Advanced Processing and Reuse of Nonferrous Metals, Lanzhou University of Technology, Lanzhou Gansu 730050, P. R. China*
[2]*School of Materials Science and Engineering, Lanzhou University Technology, Lanzhou Gansu 730050, P. R. China*

Received 4 August 2020, received in revised form 9 October 2020, accepted 18 February 2021

Abstract

In this work, ø 3 mm × 70 mm $(Zr_{63.36}Cu_{14.52}Ni_{10.12}Al_{12})_{1-x}Y_x$ (x = 0, 0.2, 0.5, 0.6, 1, 1.2, 1.5, 2, and 3 at.%) rod-shaped bulk metallic glasses (BMGs) were fabricated using the copper mold suction casting method and the effects of the addition of Y on the properties of Zr-based BMGs were studied. The results indicate that the properties of Zr-based BMGs can be enormously improved by the addition of an appropriate amount of the rare earth Y element. The values of the supercooled liquid region width (ΔT_x), glass-forming ability (GFA) parameter (γ), thermoplastic forming (TPF) ability parameter (S), and plastic strain (ε_p) for the alloy with $x = 0.6$ reach 115 K, 0.390, 0.228, and 16.5 %, respectively, and are much higher than those of the alloy with $x = 0$, indicating that the alloy with $x = 0.6$ exhibits excellent thermal stability, glass-forming ability, thermoplastic forming ability, and compressive plasticity. It was also found that the alloy with $x = 1.5$ has the minimum corrosion current (i_{corr} = 1.12 × 10^{-9} A cm^{-2}), showing excellent corrosion resistance. Overall, the alloy with the Y content of $x = 0.6$ demonstrates excellent thermal stability, GFA, TPF ability, mechanical properties, and corrosion resistance, thus displaying improved comprehensive properties.

K e y w o r d s: bulk metallic glass, rare earth Y, glass-forming ability, plastic strain, corrosion resistance

1. Introduction

The demand for microelectronic parts in the microelectromechanical systems (MEMS) is increasing continuously. However, due to the existence of grains inside the ordinary crystalline materials, the application of microdevices has been restricted by the grain size, and ordinary crystalline materials have not been able to meet the needs of miniaturized parts. Zr-based bulk metallic glasses (BMGs) do not display the grain-induced scale effect and have excellent properties such as high strength, high hardness, low Young's modulus and high abrasion resistance [1–6]. They also have good thermoplastic properties in the supercooled liquid region [7, 8], making them ideal materials for MEMS applications. However, it is well-known that BMGs are quite brittle at room temperature and are prone to crystallize in the forming process at high temperature, limiting the use of BMGs in microforming technology. Therefore, to obtain amorphous alloy compositions with high plasticity, thermal stability and other properties, many researchers have tried to further improve specific properties of the existing high-performance amorphous alloy systems. In particular, microalloying is a general and effective method for enhancing alloy properties [9].

It was found that an addition of an appropriate amount of Ti to Zr-based BMGs can significantly improve the glass-forming ability (GFA), plasticity, and compressive fracture strength of the BMGs [10, 11]. In contrast, the addition of Cr to Fe-Si-B amorphous alloys was shown to improve their thermal stability, soft magnetic properties, and corrosion resistance [12, 13]. Furthermore, it was demonstrated that the amorphous component could be obtained with excellent strength, plasticity and corrosion resistance when a

*Corresponding author: e-mail address: licywz@163.com

moderate amount of Ta is added into Zr-based BMGs [14]. Also, rare earth elements known as "industrial vitamins" because of their unique excellent magnetic, optical, and electrical properties can show a tremendous effect of improving product performance. Therefore, they have received intense attention to improving the properties of amorphous alloys. It has been discovered that rare earth elements affect purifying the melt and improving the GFA and oxidation resistance [15, 16]. For example, a small amount of Ce added to the Al-Co amorphous alloys can significantly enhance its corrosion effect [17]. In contrast, Er can improve the GFA and mechanical properties of Zr-based BMGs [18]. Besides, low-cost rare earth Y has been considered to be a good material for microalloying. The addition of Y can not only improve the GFA and manufacturability of Zr-based BMGs [16], but also enhances their corrosion resistance performance [19]. Moreover, the Cu-Zr-Al BMG with added rare-earth Y displays smaller flow stress, indicating that it is more suitable for forming at high temperature [20].

However, few studies have studied the effect of Y addition on the comprehensive properties of Zr-based BMGs. Therefore, in this work, to identify BMG compositions with excellent comprehensive performance, Zr-Cu-Ni-Al $(Zr_{63.36}Cu_{14.52}Ni_{10.12}Al_{12})_{1-x}Y_x$ ($x = 0$, 0.2, 0.5, 0.6, 1, 1.2, 1.5, 2, and 3 at.%). BMGs were fabricated by the copper mold suction casting method. The effects of Y on the thermal stability, GFA, mechanical properties and corrosion resistance of the alloy were studied systematically [21–25].

2. Methods

Alloy ingots of $(Zr_{63.36}Cu_{14.52}Ni_{10.12}Al_{12})_{1-x}Y_x$ ($x = 0$, 0.2, 0.5, 0.6, 1, 1.2, 1.5, 2, and 3 at.%) were prepared by electro-magnetic induction smelting of a mixture of high-purity Zr (99.95 %), Cu (99.99 %), Ni (99.95 %), Al (99.99 %), and Y (99.99 %) under highly pure argon atmosphere. The master alloys were remelted at least three times to ensure the composition uniformity. The alloy rod samples with a diameter of 3 mm were fabricated by the copper mold suction casting method. The internal structure was examined by X-ray diffraction (XRD) (D/max-2400, Cu Kα radiation) in the diffraction angle range of 20°–80° and transmission electron microscopy (TEM, FEI Talos F200X). The glass transition and crystallization behavior of the sample were evaluated by differential scanning calorimetry (DSC, NETZSCH DSC 204, Germany) under argon atmosphere with a heating rate of 20 $K\,s^{-1}$. Uniaxial compression tests of ø 3 mm × 6 mm samples were performed using a WDW-100D mechanical testing machine at room temperature with a load strain rate of $1 \times 10^{-4}\,s^{-1}$. The engineering stress-strain curve of the alloy was analyzed, and the trends of the change in the plasticity and strength at room temperature were studied. The sample's fracture and shear bands morphology were observed by scanning electron microscopy (SEM, JSM-6700). The microhardness was measured with HV-1000 microhardness tester using an applied load of 200 g and hold time of 15 s. In the testing, nine points were selected in each section, and the hardness values in different areas were measured. To evaluate corrosion behavior, an electrochemical workstation (HC-600e) was used for corrosion resistance testing in a $0.5\,mol\,L^{-1}$ H_2SO_4 solution. The platinum plate electrode, saturated calomel electrode and the sample were used as the auxiliary electrode, reference electrode and working electrode, respectively. The surface of the sample with an area of $7.068\,cm^2$ was immersed in the solution for 20 min to ensure the stability of the open-circuit potential. The scanning rate for the dynamic polarization curve measurements was $1\,mV\,s^{-1}$. The corrosion morphology was observed by SEM (JSM-6700), and the distribution of the elements on the surface was detected by the energy dispersive spectroscopy (EDS).

3. Results and discussion

3.1. XRD and TEM tests results

Figure 1a shows the XRD patterns of the $(Zr_{63.36}Cu_{14.52}Ni_{10.12}Al_{12})_{1-x}Y_x$ ($x = 0$, 0.2, 0.5, 0.6, 1, 1.2, 1.5, 2, and 3 at.%) alloy samples. It is observed that most curves show a broad diffuse scattering peak with no sharp peaks corresponding to crystalline materials, indicating that the alloy basically remains amorphous structure with the addition of Y. To further identify whether the alloys contain crystals, the internal structure of $x = 0.6$ alloy was analyzed by high-resolution transmission electron microscopy (HRTEM) and selected area electron diffraction (SAED), as shown in Fig. 1b. It can be seen that the diffraction spot is aureole, and the arrangement of atoms is irregular, showing that the structure of the alloy is completely amorphous, and no crystallization occurs.

3.2. DSC test results

Figure 2 shows the DSC curves of the $(Zr_{63.36}Cu_{14.52}Ni_{10.12}Al_{12})_{1-x}Y_x$($x = 0$, 0.2, 0.5, 0.6, 1, 1.2, 1.5, 2, and 3 at.%) BMGs. The thermodynamic parameters of each alloy (glass transition temperature T_g, crystallization temperature T_x, solid-phase temperature T_m, liquid phase temperature T_l, supercooled liquid region width ΔT_x ($\Delta T_x = T_x - T_g$), γ ($\gamma = T_x/(T_g + T_l)$) and S ($S = \Delta T_x/(T_l - T_g)$) derived from the DSC curves are listed in Table 1. The thermal stability, GFA, and thermoplastic forming (TPF)

Table 1. Thermodynamic parameters of $(Zr_{63.36}Cu_{14.52}Ni_{10.12}Al_{12})_{1-x}Y_x$ (x = 0, 0.2, 0.5, 0.6, 1, 1.2, 1.5, 2, and 3 at.%) BMGs

x	T_g (℃)	T_x(℃)	T_m (℃)	T_l (℃)	ΔT_x (℃)	γ	S
0	376	471	836	859	95	0.381	0.196
0.2	375	487	837	878	112	0.388	0.222
0.5	373	469	827	860	96	0.380	0.197
0.6	372	487	833	876	115	0.390	0.228
1	380	474	838	882	94	0.375	0.187
1.2	391	483	834	872	92	0.382	0.191
1.5	392	470	843	872	78	0.371	0.163
2	384	476	818	881	92	0.374	0.185
3	375	427	803	871	52	0.342	0.104

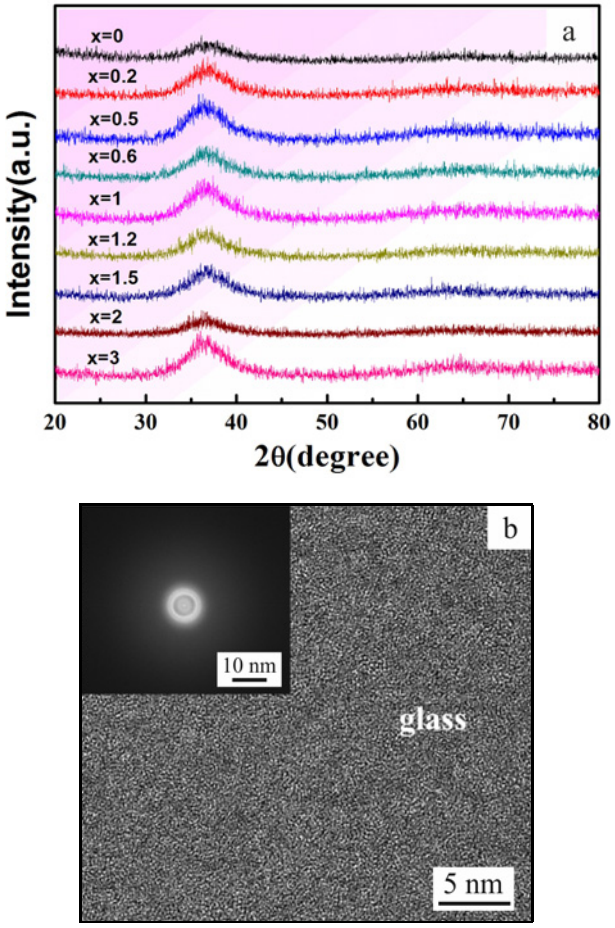

Fig. 1. (a) The XRD diffraction patterns of $(Zr_{63.36}Cu_{14.52}Ni_{10.12}Al_{12})_{1-x}Y_x$ (x = 0, 0.2, 0.5, 0.6, 1, 1.2, 1.5, 2, and 3 at.%) BMGs, (b) the HRTEM image and the SEAD (inset) of the x = 0.6 alloy.

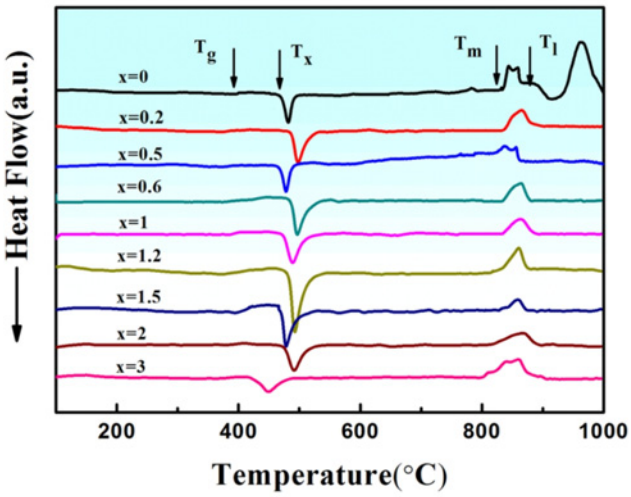

Fig. 2. The DSC curves for $(Zr_{63.36}Cu_{14.52}Ni_{10.12}Al_{12})_{1-x}Y_x$ (x = 0, 0.2, 0.5, 0.6, 1, 1.2, 1.5, 2, and 3 at.%) BMGs.

ability of amorphous metals influence their development and application, and are affected by the alloy composition and processing conditions. ΔT_x, γ, and S are generally used to assess the thermal stability, GFA and TPF ability of BMGs, respectively, and their values are affected by the T_g, T_x, and T_l of the alloy. Higher ΔT_x, γ, and S indicate better thermal stability, GFA, and TPF of the alloy that enable it to be used for a longer time for forming at high temperature. An examination of the data presented in Table 1 shows that with the increasing x, the alloy's T_g shows a trend of first decreasing, then increasing and finally decreasing again. The decrease in T_g is conducive to improving the alloy thermal stability, GFA and TPF ability. ΔT_x, γ, and S increased to the maximum values of 115°, 0.390, and 0.228, respectively, after adding an appropriate amount of Y with x = 0.6. Figure 3 shows the measured ΔT_x, S, and γ of the $(Zr_{63.36}Cu_{14.52}Ni_{10.12}Al_{12})_{1-x}Y_x$ (x = 0, 0.2, 0.5, 0.6, 1, 1.2, 1.5, 2, and 3 at.%) BMGs as a function of the Y content. It is observed that with increasing Y content, ΔT_x, S, and γ show essentially the same behavior. This indicates that alloys with good thermal stability also have high GFA and TPF ability. The BMG with x = 0.6 has the maximum values of ΔT_x = 115 K, S = 0.228, and γ = 0.381, showing the highest thermal stability and TPF ability, and the

Table 2. Mechanical properties parameters of $(Zr_{63.36}Cu_{14.52}Ni_{10.12}Al_{12})_{1-x}Y_x$ (x = 0, 0.2, 0.5, 0.6, 1, 1.2, 1.5, 2, and 3 at.%) BMGs

x	Plastic strain ε_p (%)	Yield strength σ_s (MPa)	Compressive strength) σ_{max} (MPa)	Fracture strength σ_f (MPa)
0	0.7	1673	1724	1702
0.2	5	1726	1892	1905
0.5	15.1	1664	1883	1848
0.6	16.5	1630	1892	1784
1	17.6	1700	2041	1683
1.2	4.6	1533	1673	1667
1.5	5.1	1599	1710	1597
2	5.8	1638	1848	1663
3	0	1653	1653	1653

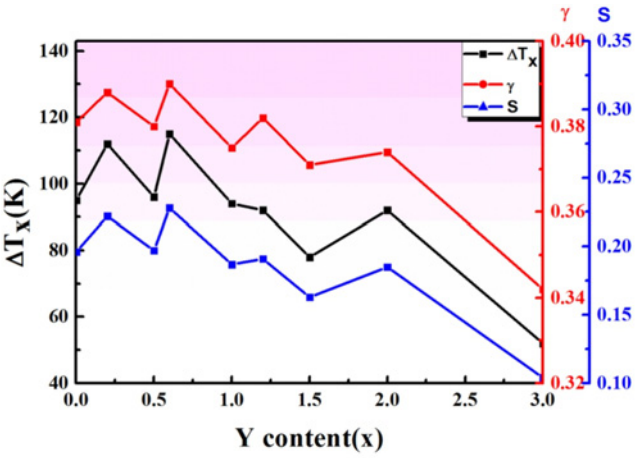

Fig. 3. The curves of ΔT_x, γ, and S with the Y content (x) (x = 0, 0.2, 0.5, 0.6, 1, 1.2, 1.5, 2, and 3 at.%).

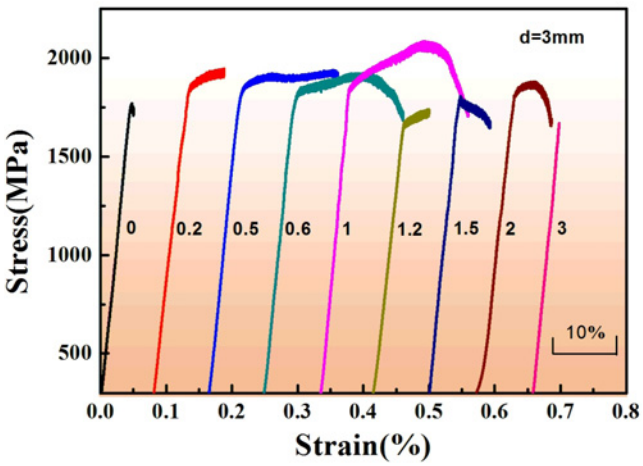

Fig. 4. Compressive stress–strain curves of $(Zr_{63.36}Cu_{14.52}Ni_{10.12}Al_{12})_{1-x}Y_x$ (x = 0, 0.2, 0.5, 0.6, 1, 1.2, 1.5, 2, and 3 at.%) BMGs.

best GFA among the examined alloys. Therefore, the alloy composition of $x = 0.6$ is not only more suitable for obtaining an amorphous structure but also is more suitable for thermoplastic forming. As x increases to 3, the alloy's ΔT_x is only 52 K, and γ and S also drop sharply, so that the TPF ability and GFA decrease rapidly. This shows that an addition of a small amount of rare earth Y can not only significantly improve the thermal stability and GFA of the Zr-based BMG, but also greatly enhances its TPF ability.

3.3. Stress-strain curve and fracture appearance analysis

The stress-strain curves of the $(Zr_{63.36}Cu_{14.52}Ni_{10.12}Al_{12})_{1-x}Y_x$ (x = 0, 0.2, 0.5, 0.6, 1, 1.2, 1.5, 2, and 3 at.%) BMGs are shown in Fig. 4, and the compressive plastic strain (ε_p), yield strength (σ_s), compressive strength (σ_{max}), and fracture strength (σ_f) of each sample derived from the stress-strain curves are listed in Table 2. It is observed from Fig. 4 that the sample with $x = 0$ shows a brittle fracture, and its ε_p is only 0.7 %. With increasing Y content, the compressive plastic strain of the alloy first increased and then decreased. When x increased to 1, ε_p reached the maximum value of 17.6 %, which is 25 times higher than that of the alloy with $x = 0$. Meanwhile, σ_s and σ_{max} also reached their maximum values. As the Y content increases further to $x = 1.2$, the ε_p, σ_s, σ_{max}, and σ_f all decrease sharply. The plastic strain is basically stable at approximately 5 % between $x = 1.2$ and $x = 2$. When x increases to 3, $\varepsilon_p = 0$, indicating that the sample breaks directly after elastic deformation without the yielding stage. These results show that the compressive plasticity of Zr-based BMGs at room temperature can be greatly improved by the addition of an appropriate amount of Y. Furthermore, the amorphous alloy with $x = 0.6$ not only has the best GFA and TPF but also has a large plastic strain with $\varepsilon_p = 16.5$ %. Therefore, the Zr-based BMG with $x = 0.6$ has the best potential for development and applications.

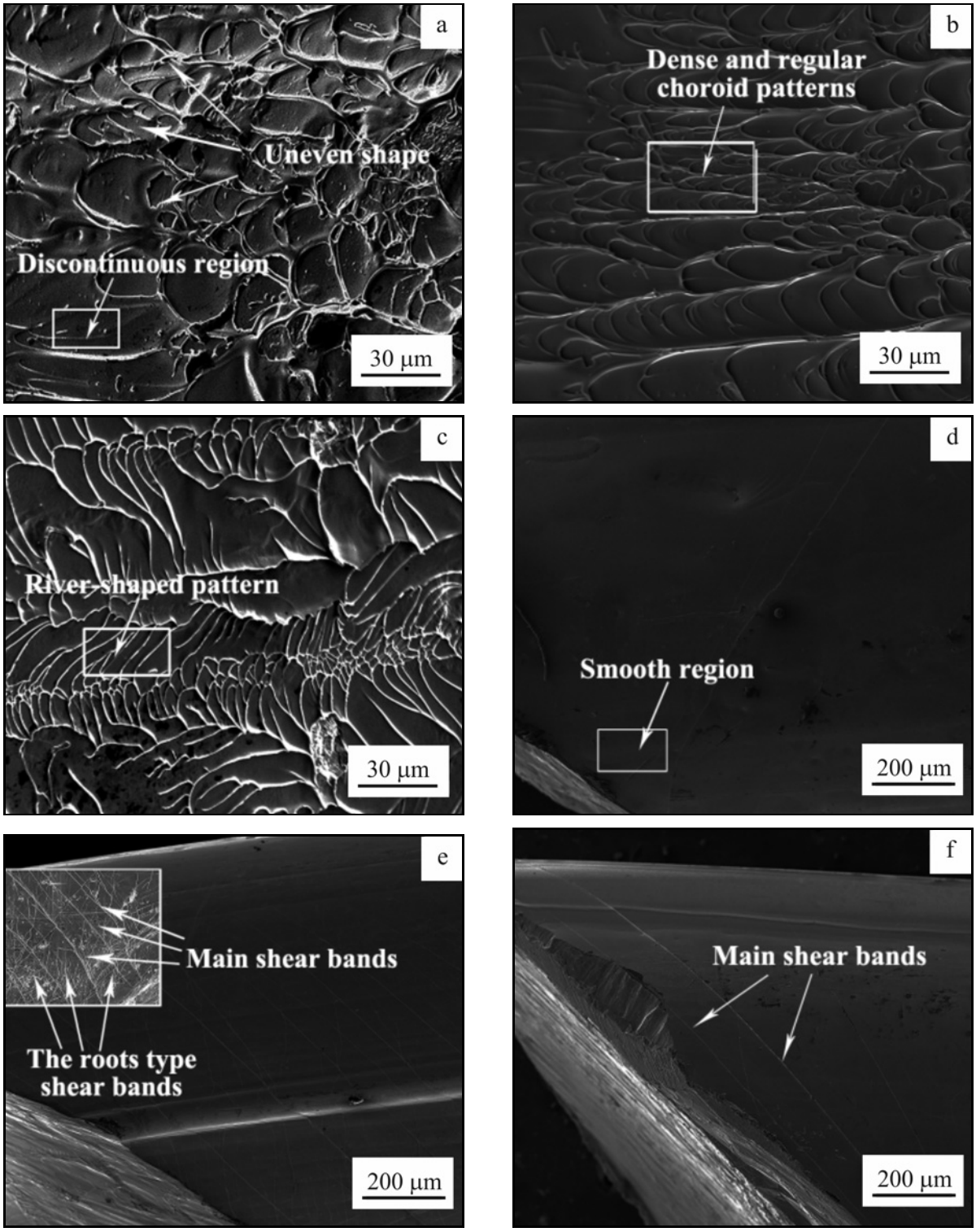

Fig. 5. The fracture morphology and shear band morphology of compression fracture: (a), (d) $x = 0$, (b), (e) $x = 0.6$, and (c), (f) $x = 2$.

The plastic deformation of BMG is thought to be achieved by the local redistribution of atomic clusters. Therefore, the plastic deformation of BMGs is mainly controlled by the fracture topography and the density and distribution of shear bands rather than by the free volume [26]. Previous studies have shown that the number of vein-like patterns on the fracture surface determines the plasticity of BMGs [27]. The fracture and shear band morphology of the alloy samples after compression are shown in Fig. 5. In particu-

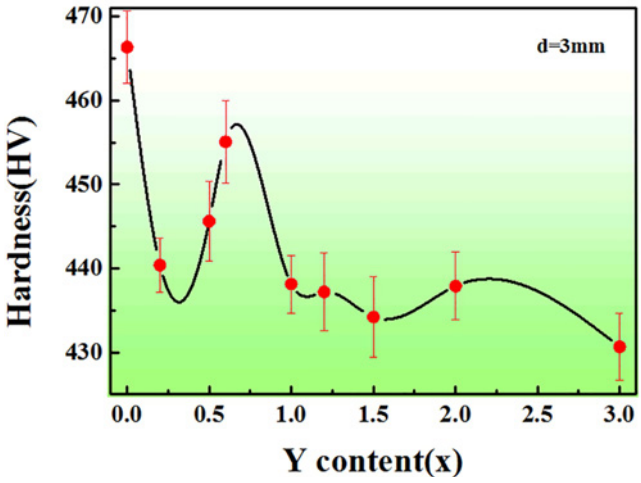

Fig. 6. The microhardness of $(Zr_{63.36}Cu_{14.52}Ni_{10.12}Al_{12})_{1-x}Y_x$ (x = 0, 0.2, 0.5, 0.6, 1, 1.2, 1.5, 2, and 3 at.%) BMGs.

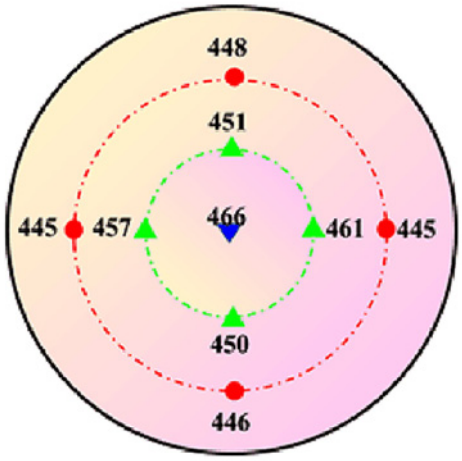

Fig. 7. Microhardness distribution on cross section of $(Zr_{63.36}Cu_{14.52}Ni_{10.12}Al_{12})_{1-x}Y_x$ (x = 0.6).

lar, Figs. 5a and 5d show respectively the fracture and shear band morphology of the alloy sample with $x = 0$. It is observed that the vein-like pattern on the surface is discontinuous, and its shape is uneven (Fig. 5a). The fracture side is also relatively smooth, and virtually no shear band is generated (Fig. 5d). This indicates that after the alloy reaches the elastic limit under pressure, the stress is highly concentrated, and the alloy breaks quickly, showing typical brittle fracture characteristics. By contrast, as shown in Figs. 5b and 5e, when Y content increases to $x = 0.6$, the fracture of the alloy presents dense and regular lamellar vein-like patterns with shapes similar to that of the traditional BMG section (Fig. 5b) [28]. The dense shear bands from the sample's side can also be observed, including main shear bands and a large number of the roots-type shear bands (inset of Fig. 5e)). This shows that during the compression, the energy accumulated in the alloy is continuously released through the complicated and dense shear bands, indicating excellent room-temperature compression plasticity. Figures 5c and 5f show respectively the fracture and shear band morphology of the alloy with $x = 2$. It is observed from Fig. 5c that many dense river-like patterns are present in the sample. It is generally considered that the river-shaped pattern is a secondary or tertiary shear band [28, 29]. It only has a small number of main shear bands on the specimen's side, demonstrating brittle fracture characteristics, as shown in Fig. 5f.

3.4. Microhardness analysis

The microhardness was measured for the samples with different compositions, with the results shown in Fig. 6. It is observed that the highest microhardness (466 HV) was obtained for the alloy with x = 0. Upon adding a small amount of rare earth Y (x = 0.2), the hardness decreased dramatically. With the further increase of the Y content, the microhardness first increased and then decreased, reaching the maximum value at $x = 0.6$ (456 HV) and the minimum value at $x = 3$ (430 HV). It is observed that the hardness of the alloy with added Y is lower than that of $x = 0$, indicating that the addition of rare earth Y is not conducive to improving the hardness of the Zr-based BMG. This may be because the addition of Y increases the alloy's liquid viscosity, endowing with a more disordered atomic arrangement and greater free volume than the alloy with $x = 0$, leading to a decreased hardness. In addition to the influence of the alloy composition, the microhardness of the amorphous alloy is also strongly affected by the cooling rate because the generation of the free volume is proportional to the cooling rate [30]. Figure 7 shows a schematic diagram of the hardness values in the different areas of $(Zr_{63.36}Cu_{14.52}Ni_{10.12}Al_{12})_{1-x}Y_x$ (x = 0.6). It is observed that the hardness of the alloy increases continuously from the edge region to the central region, showing an obvious hardness gradient. The core of the sample displays the highest hardness of 466 HV. This is because, during the suction casting process, the alloy's edge regions are in direct contact with the copper mold, giving rise to a higher cooling rate, a more disordered internal atomic arrangement, and a higher free volume.

To comprehensively compare the mechanical properties of $(Zr_{63.36}Cu_{14.52}Ni_{10.12}Al_{12})_{1-x}Y_x$ (x = 0, 0.2, 0.5, 0.6, 1, 1.2, 1.5, 2, and 3 at.%) BMGs, the compressive plastic strain, compressive fracture strength, and Vickers hardness of all alloy samples were summarized and analyzed, as shown in Fig. 8. The mechanical properties of the alloy can be divided into three regions: the unbalanced performance region (I), the balanced performance region (II), and the

Table 3. Electrochemical parameters of $(Zr_{63.36}Cu_{14.52}Ni_{10.12}Al_{12})_{1-x}Y_x$ (x = 0, 0.2, 0.5, 0.6, 1, 1.2, 1.5, 2, and 3 at.%) BMGs derived from polarization curves

Y content (x)	E_{corr} (V)	i_{corr} (A cm^{-2})
0	–0.21	3.24×10^{-8}
0.2	–0.05	6.83×10^{-7}
0.5	–0.30	4.29×10^{-8}
0.6	–0.18	2.73×10^{-8}
1	–0.10	1.2×10^{-7}
1.2	–0.21	1.80×10^{-8}
1.5	–0.29	1.12×10^{-9}
2	–0.23	2.61×10^{-8}
3	–0.20	2.81×10^{-8}

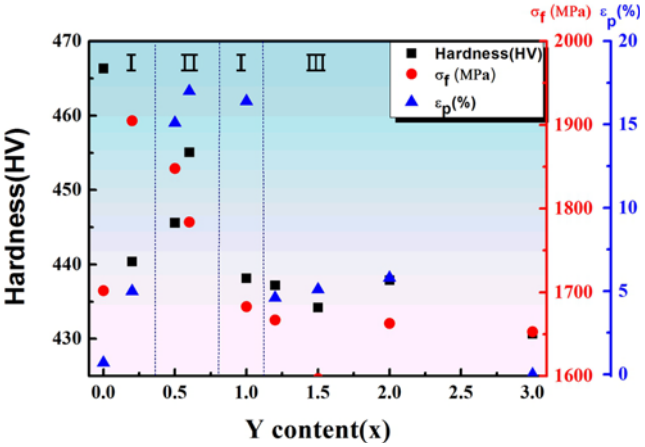

Fig. 8. Plastic strain and microhardness of $(Zr_{63.36}Cu_{14.52}Ni_{10.12}Al_{12})_{1-x}Y_x$ (x = 0, 0.2, 0.5, 0.6, 1, 1.2, 1.5, 2, and 3 at.%).

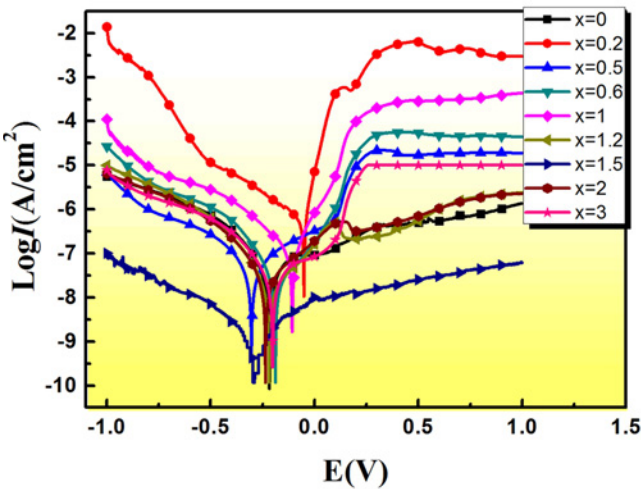

Fig. 9. Tafel curves of $(Zr_{63.36}Cu_{14.52}Ni_{10.12}Al_{12})_{1-x}Y_x$ (x = 0, 0.2, 0.5, 0.6, 1, 1.2, 1.5, 2, and 3 at.%).

low-performance region (III). The compressive plastic strain, compressive fracture strength, and Vickers hardness of the alloy in the region I are uneven, with some properties showing high values and the rest of the properties showing highly unfavorable values. The alloy's hardness value is the highest in the absence of Y (x = 0), and its strength and plastic strain are relatively low, showing obvious hard brittleness. In contrast, for x = 0.2, the highest fracture strength is obtained, but its hardness and plastic strain values are small. The alloy with x = 1 displays the highest plasticity at room temperature, but its strength and hardness are low, showing the performance relationship of typical traditional crystal materials. Region II only contains alloys with x = 0.5 and x = 0.6. These two alloys show high strength, hardness, and large plastic strain, greatly improving the room-temperature brittleness, and have good comprehensive mechanical properties. The alloys in the region III have a relatively low plastic strain, compressive strength and hardness, and the alloy's overall performance is the worst when Y content increases to x = 3. This indicates that the excessive addition of Y deteriorates the mechanical properties of Zr-based BMGs. To summarize, the addition of an appropriate content of the rare earth element Y (x = 0.5 and x = 0.6) greatly improves the comprehensive mechanical properties of Zr-based BMGs.

3.5. Electrochemical behavior

The potentiodynamic polarization curves of $(Zr_{63.36}Cu_{14.52}Ni_{10.12}Al_{12})_{1-x}Y_x$ (x = 0, 0.2, 0.5, 0.6, 1, 1.2, 1.5, 2, and 3 at.%) BMGs are shown in Fig. 9. It is observed that except for the alloy with x = 1.5, all other amorphous alloys are spontaneously passivated by anodic polarization, accompanied by a wider passivation range and subsequent pitting at higher potentials. The corrosion potential (E_{corr}) and corrosion current density (i_{corr}) parameters obtained from the polarization curves are listed in Table 3. It is observed that all Y-containing BMGs have similar potentials, except for the alloys with x = 0.2 and x = 1. This indicates that most Y-containing alloys have approxi-

Table 4. The atomic percentage of elements on crater (at.%)

Y	O	Zr	Cu	Ni	Al	S	Total
31.1	18.3	24.2	10.1	7.7	6.1	2.5	100

mately the same corrosion tendency as the alloy with $x = 0$. For a more accurate evaluation of the alloy's corrosion resistance, the change in the corrosion current density was analyzed. It is observed that for most of the alloys, including the alloy with $x = 0$, higher corrosion resistance values are obtained, but the corrosion current density values were still on the order of 10^{-8}A cm^{-2}. It was also found that the alloy with $x = 0.2$ has the largest corrosion current density, the fastest corrosion rate, and the lowest corrosion resistance, while the corrosion current density of the alloy with $x = 1.5$ is the lowest, reaching an order of magnitude of 10^{-9}A cm^{-2}. It is also observed from Fig. 9 that the curve for this alloy shows no obvious pitting phenomenon, indicating that the alloy has excellent corrosion resistance. However, the improvement of corrosion resistance of BMGs is not consistent with the trends for the mechanical properties, and the mechanical properties of the alloy with $x = 1.5$ are not improved.

The corrosion morphologies of the alloys $x = 0.2$ and $x = 1.5$ are shown in Figs. 10a and 10b, respectively. It is observed that the surface of the alloy with $x = 1.5$ was not damaged after the corrosion, and the surface is smooth without any corrosion marks. This indicates that the passivation film formed on the alloy surface has good corrosion resistance, consistent with the result derived from the corrosion curve. By contrast, the alloy with $x = 0.2$ shows poor corrosion resistance, and obvious corrosion pits appear on the surface due to pitting corrosion. The distribution of the elements on the surface of the corrosion pits is shown in Fig. 11. It is observed that there are two parts in the corrosion pit area, namely the flat and smooth sag area on the bottom and the incomplete sag area with a rough surface. This indicates that some passivated layers are destroyed after pitting, while the passivated film in the incomplete sag area is only partially destroyed. Examination of the elemental distribution shows that Y (31.1 at.%), Zr (18.3 at.%), O (24.2 at.%), and Al (6.1 at.%) are abundant in the incomplete sag area, indicating that Y, Zr, and Al reacted with O atoms and formed a passivation film with high corrosion resistance during the corrosion. Because Y has a higher Fermi level and lower electrode potential than Zr and Al, Y atoms react more easily with O to form the passivation film than Zr and Al [31]. In the sag area, the O content is quite low, and the passivation film is destroyed. These results show that Y plays an active role in forming the passivation film during the corrosion of Zr-based BMGs.

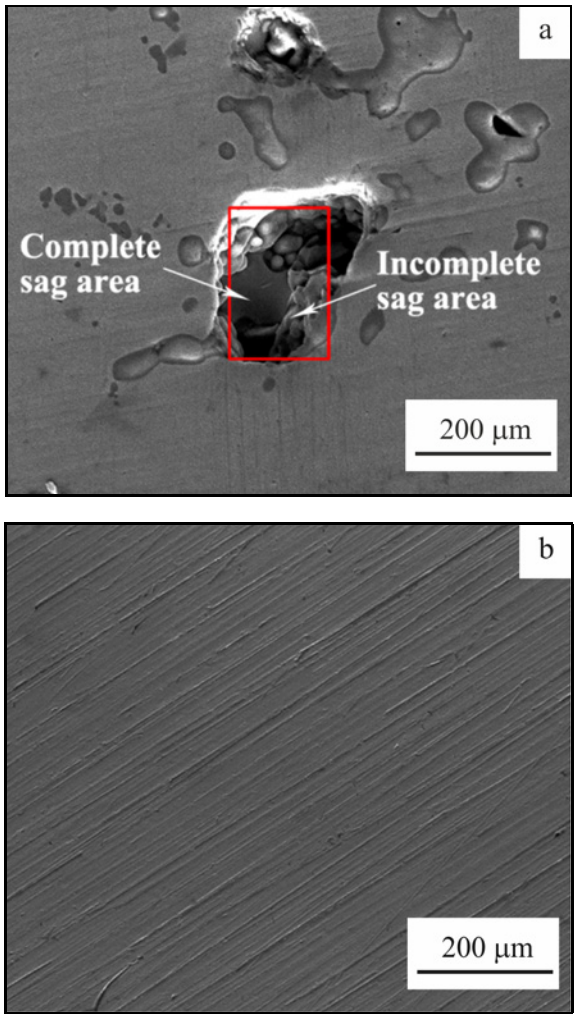

Fig. 10. Surface corrosion morphology of BMGs for (a) $x = 0.2$ and (b) $x = 1.5$.

4. Conclusions

In this work, $(Zr_{63.36}Cu_{14.52}Ni_{10.12}Al_{12})_{1-x}Y_x$ ($x = 0$, 0.2, 0.5, 0.6, 1, 1.2, 1.5, 2, and 3 at.%) BMGs were obtained by the copper mold casting method and show an amorphous structure with no crystallization. The addition of an appropriate amount of Y significantly improves the properties of Zr-based BMGs. The values of the supercooled liquid region width ΔT_x, γ, S, and plastic strain ε_p for the alloy with $x = 0.6$ reach 115 K, 0.390, 0.228, and 16.5 %, respectively, and are much higher than those of the alloy with $x = 0$, indicating that the alloy with $x = 0.6$ exhibits excellent thermal stability, GFA, TPF ability,

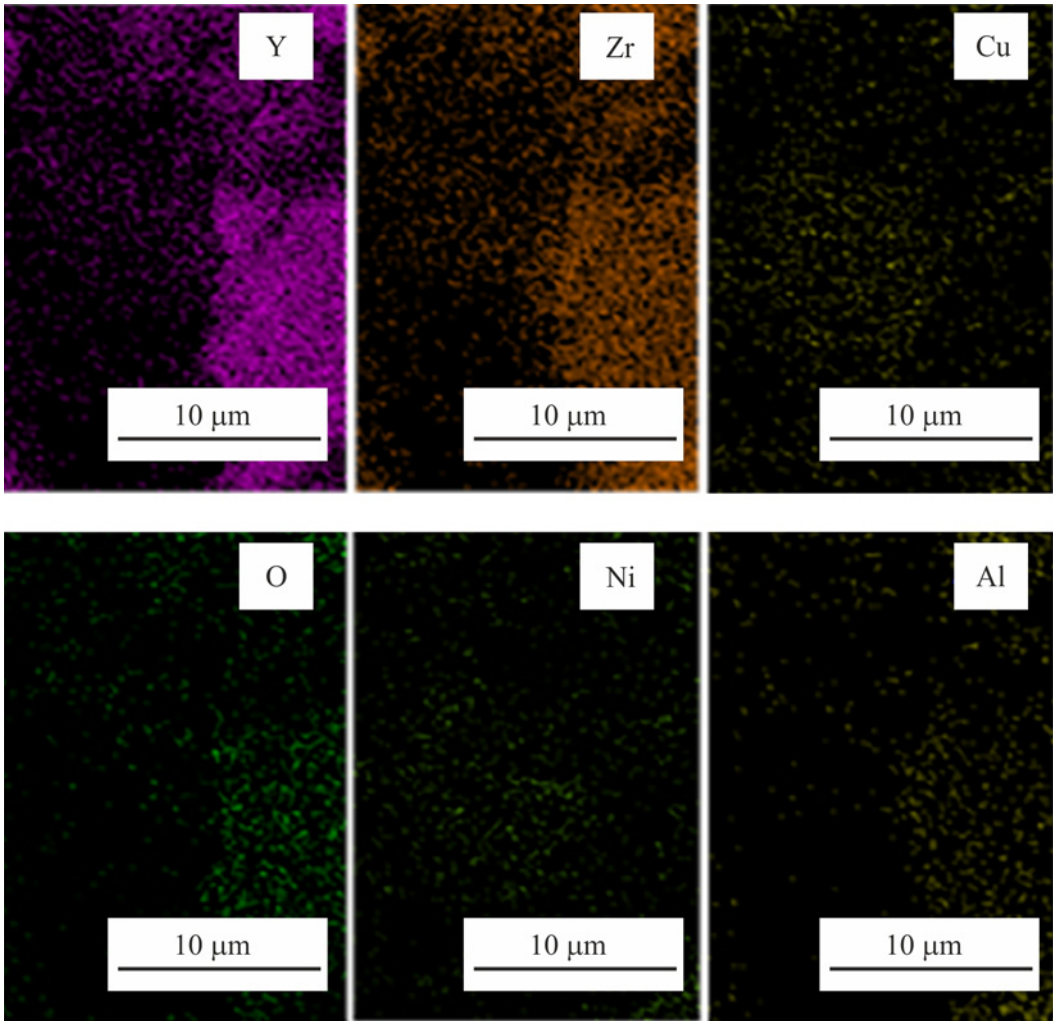

Fig. 11. Distribution of elements on the surface of corrosion pits.

and compressive plasticity. Also, the addition of an appropriate Y amount is conducive to the formation of a passivation film on the alloy surface and therefore improves the corrosion resistance. The alloy with $x = 1.5$ displays the minimum current density ($i_{corr} = 1.12 \times 10^{-9}$ A cm^{-2}), showing excellent corrosion resistance.

Acknowledgements

The authors like to gratefully acknowledge the National Natural Science Foundation of China (51661016, 51861021, 51571105) and Hongliu First-Class Discipline Construction Plan of Lanzhou University of Technology.

References

[1] A. Inoue, Stabilization of metallic supercooled liquid and bulk amorphous alloys, Acta Materialia 48 (2000) 279–306. doi:10.1016/S1359-6454(99)00300-6

[2] A. L. Greer, E. Ma, Bulk metallic glasses: At the cutting edge of metals research, MRS Bull 32 (2007) 611–615. doi:10.1557/mrs2007.121

[3] Y. Yokoyama, K. Fujita, A. R. Yavari, A. Inoue, Malleable hypoeutectic Zr-Ni-Cu-Al bulk glassy alloys with tensile plastic elongation at room temperature, Philosophical Magazine Letters 89 (2009) 322–334. doi:10.1080/09500830902873575

[4] X. Hui, S. N. Liu, S. J. Pang, L. C. Zhuo, T. Zhang, G. L. Chen, Z. K. Liu, High-zirconium-based bulk metallic glasses with large plasticity, Scripta Materialia 63 (2010) 239–242. doi: 10.1016/j.scriptamat.2010.03.065

[5] J. Pan, K. C. Chan, Q. Chen, L. Liu, Enhanced plasticity by introducing icosahedral medium-range order in ZrCuNiAl metallic glass, Intermetallics 24 (2012) 79–83. doi: 10.1016/j.intermet.2012.01.006

[6] N. B. Hua, W. Z. Chen, X. L. Liu, F. Yue, Isochronal and isothermal crystallization kinetics of Zr-Al-Fe glassy alloys: Effect of high-Zr content, Non-Cryst. Solids 388 (2014) 10–16. doi: 10.1016/j.jnoncrysol.2014.01.013

[7] G. Kumar, H. X. Tang, J. Schroers, Nanomoulding with amorphous metals, Nature, 457 (2009) 868–872. doi:10.1038/nature07718

[8] J. Schroers, Processing of bulk metallic glass, Advanced Materials 22 (2007) 1566–1597. doi: 10.1002/adma.200902776
[9] W. H. Wang, Roles of minor additions in formation and properties of bulk metallic glasses, Progress in Materials Science 52 (2007) 540–596. doi: 10.1016/j.pmatsci.2006.07.003
[10] Y. Zhang, J. Yao, X. Zhao, L. Ma, Ti substituted Ni-free $Zr_{65-x}Ti_xCu_{17.5}Fe_{10}Al_{7.5}$ bulk metallic glasses with significantly enhanced glass-forming ability and mechanical properties, Journal of Alloys and Compounds 773 (2019) 713. doi: 10.1016/j.jallcom.2018.09.292
[11] H. Q. Shi, W. B. Zhao, X. W. Wei, Y. Ding, X. D. Shen, W. J. Liu, Effect of Ti addition on mechanical properties and corrosion resistance of Ni-free Zr-based bulk metallic glasses for potential biomedical applications, Journal of Alloys and Compounds 815 (2020) 152636. doi: 10.1016/j.jallcom.2019.152636
[12] D. D. Xu, B. L. Zhou, Q. Q. Wang, J. Zhou, W. M. Yang, C. C. Yuan, L. Xue, X. D. Fan, L. Q. Ma, B. L. Shen, Effects of Cr addition on thermal stability, soft magnetic properties and corrosion resistance of FeSiB amorphous alloys, Corrosion Science 138 (2018) 20–27. doi: 10.1016/j.corsci.2018.04.006
[13] B. Xiong, X. Li, J. B. Zheng, X. N. Li, G. H. Lu, Z. M. Wang, D. Y. Ju, A. Makino, Effect of Cr element on glass forming ability and corrosion resistance of Fe-based bulk amorphous alloys. Rare Metal Materials and Engineering 47 (2018) 701–704.
[14] T. H. Li, Y. C. Liao, S. M. Song, Y. L. Jiang, P. H. Tsai, J. S. C. Jang, J. C. Huang, Significantly enhanced mechanical properties of ZrAlCo bulk amorphous alloy by microalloying with Ta, Intermetallics 93 (2018) 162–168. doi: 10.1016/j.intermet.2017.12.008
[15] K. R. Lim, J. M. Park, S. J. Kim, E. S. Lee, W. T. Kim, A. Gebert, J. Eckert, D. H. Kim, Enhancement of oxidation resistance of the supercooled liquid in Cu-Zr-based metallic glass by forming an amorphous oxide layer with high thermal stability, Corrosion Science 66 (2013) 1–4. doi: 10.1016/j.corsci.2012.09.018
[16] L. Deng, B. W. Zhou, H. S. Yang, X. Jiang, B. Y. Jiang, X. G. Zhang, Roles of minor rare-earth elements addition in formation and properties of Cu-Zr-Al bulk metallic glasses, Journal of Alloys and Compounds 632 (2015) 429–434. doi: 10.1016/j.jallcom.2015.01.036
[17] L. M. Zhang, S. D. Zhang, A. L. Ma, A. J. Umoh, H. X. Hu, Y. G. Zheng, B. J. Yang, J. Q. Wang, Influence of cerium content on the corrosion behavior of Al-Co-Ce amorphous alloys in 0.6 M NaCl solution, Journal of Materials Science and Technology 35 (2019) 137–1387. doi: 10.1016/j.jmst.2019.03.014
[18] C. Y. Li, J. F. Yin, J. Q. Ding, F. P. Zhu, Y. C. Zhao, S. Z. Kou, Effect of Er on properties of Zr-based bulk metallic glasses, Materials Science and Technology 34 (2018) 1887–1892. doi: 10.1080/02670836.2018.1495902
[19] R. Y. Li, Z. Z. Yuan, J. Kang, X. Y. Zhang, Effects of yttrium additions on corrosion behavior of $Zr_{56}Co_{28}Al_{16}$ bulk metallic glasses in simulated body fluid, Journal of Functional Materials 47 (2016) 01159–01162. doi:10.3969/j.issn.1001-9731.2016.01.032
[20] K. Yang, X. Fan, B. Li, Y. Li, X. Wang, X. Xu, Effect of yttrium addition on the flow behavior of Cu-Zr-Al bulk metallic glass in the supercooled liquid region, Journal of Rare Earths 35 (2017) 1035–1041. doi: 10.1016/S1002-0721(17)61010-X
[21] C. Li, S. Kou, Y. Zhao, X. Yuan, Z. Yuan, Mechanical properties of Zr-based bulk metallic glasses with different Al contents, Chinese Journal of Rare Metals 39 (2015) 300–307. doi: 10.13373/j.cnki.cjrm.2015.04.002
[22] C. Y. Li, S. Z. Kou, G. Q. Liu, Effects of Fe on glass forming ability, thermal stability and mechanical properties of Zr-based alloys, Rare Metal Materials And Engineering 41 (2012) 1790–1794. doi: 10.1163/016942411X576518
[23] C. Li, S. Kou, Y. Zhao, G. Liu, Y. Ding, Effect of cooling rate on plastic deformation of Zr-based bulk metallic glasses, Progress in Natural Science 22 (2012) 21–25. doi: 10.1016/j.pnsc.2011.12.004
[24] C. Li, J. Yin, J. Ding, F. Zhu, Y. Zhao, S. Kou, Effect of Zr and Cu on mechanical properties, glass forming ability and thermal stability of $Zr_{63.68}Cu_{16.2}Ni_{10.12}Al_{10}$ amorphous alloy, Chinese Materials Conference, Advanced Functional Materials, (2017), pp. 225–238. ISBN 978-981-13-0110-0 doi:10.1007/978-981-13-0110-0_26
[25] C. Y. Li, J. F. Yin, Z. Wang, S. Z. Kou, Y. C. Zhao, Effect of Er on structure, mechanical properties, thermal stability and amorphous forming ability of ZrCuNiAl amorphous alloy, Journal of Materials Engineering 46 (2018) 1–7. doi:10.11868/j.issn.1001-4381.2016.001421
[26] J. Y. Lee, K. H. Han, M. Park, K. Chattopadhyay, W. T. Kim, D. H. Kim, Deformation and evolution of shear bands under compressive loading in bulk metallic glasses, Acta Materialia 54 (2006) 5271–5279. doi: 10.1016/j.actamat.2006.07.014
[27] Z. F. Zhang, G. He, J. Eckert, L.Schultz, Fracture mechanisms in bulk metallic glassy materials, Physical Review Letters 91 (2003) 045505. doi: 10.1103/PhysRevLett.91.045505
[28] X. K. Xi, D. Q. Zhao, M. X. Pan, W. H. Wang, Y. Wu, J. J. Lewandowski, Fracture of brittle metallic glasses: Brittleness or plasticity, Physical Review Letters 94 (2005) 125510. doi: 10.1103/PhysRevLett.94.125510
[29] M. Kusy, U. Kühn, A. Concustell, Fracture surface morphology of compressed bulk metallic glass-matrix-composites and bulk metallic glass, Intermetallics 14 (2006) 982–986. doi: 10.1016/j.intermet.2006.01.017
[30] M. Sadeghilaridjani, A. Ayyagari, S. Muskeri, V. Hasannaeimi, S. Mukherjee, Small-scale mechanical behavior of ion-irradiated bulk metallic glass, The Journal of The Minerals, Metals & Materials Society 72 (2020) 123–129. doi: 10.1007/s11837-019-03848-3
[31] H. Zhang, G. Y. Zhang, S. Yang, D. Wu, K. Z. Qi, Effects of additional element on the glass forming ability and corrosion resistance of bulk Zr-based amorphous alloys, Acta Physica Sinica 57 (2008) 7822–7826. doi:10.7498/aps.57.7822